A biophysical model of synaptic tagging-and-capture based on actin dynamics

Negri, Francesco[1◕], Luboeinski, Jannik[1,2,3◕], Tetzlaff, Christian[1,3], Fauth, Michael[2,3]

1 Department for Neuro- and Sensory Physiology, University of Göttingen Medical Center, Göttingen, Germany
2 III. Institute of Physics – Biophysics, University of Göttingen, Göttingen, Germany
3 Bernstein Center for Computational Neuroscience, Göttingen, Germany

◕These authors contributed equally to this work.
¤a Current Address: III. Institute of Physics – Biophysics, University of Göttingen, Friedrich-Hund-Platz 1, 37077 Göttingen, Germany
* mfauth@gwdg.de

Abstract

According to the synaptic tagging-and-capture hypothesis, long-lasting (late-phase) plasticity requires the synthesis of plasticity-related proteins and the setting of a synaptic tag at the stimulated synapse. It has been hypothesized that this tag is implemented by the complex interplay between dendritic spine geometry and the scaffolding protein actin.

To test this, we propose a biophysically-grounded model of late-phase synaptic plasticity considering dynamic and stable actin pools and the size of the PSD in the synapse. In our model, the tag corresponds to the imbalance between the spine volume determined by actin and the volume that would be expected for the current PSD size.

We demonstrate the viability of the proposed model by showing that it can account for the experimentally observed synaptic plasticity induced by stimulation of a single synapse, as well as tag-resetting protocols, and heterosynaptic plasticity protocols involving two synapses.

Moreover, for the interaction of two consecutive stimuli at the same synapse within around up to an hour, plastic changes stack non-linearly, reminiscent of the spacing effect found in learning and memory studies.

In summary, our model both matches experiments and extrapolates well to a wide range of stimulation protocols. Thus, it will be ideally suited to serve as a basis to predict the plasticity effects emerging from the complex activity patterns in recurrent networks.

Introduction

Synaptic Tagging-and-Capture Synapses and their adaptation through synaptic plasticity are believed to be the underpinning for learning and memory [1]. The most prominent forms of synaptic plasticity are long-term potentiation (LTP, [2]) and long-term depression (LTD, [3]). Both have been found to have at least two major phases [4]: an early phase with changes in synaptic transmission efficacy based on altered receptor trafficking, which quickly decay; and a long-lasting phase based on a reorganization of the synapse structure which persists for hours. According to the

synaptic tagging-and-capture hypothesis, this long-lasting phase only occurs if two factors are present [5, 6]: (i) plasticity-related products (PRPs), e.g., *de novo* synthesized proteins, that can be captured by the synapses and used for restructuring, and (ii) a so-called synaptic tag that provides a short-term memory of which synapses have undergone early-phase plasticity and enables them to capture the PRPs. These components are independent as, for example, a tag can be set without triggering PRPs synthesis but still enables a synapse to capture PRPs while they are present [5]. Furthermore, also the impact of subsequent plasticity-inducing stimuli strongly depends on whether and when PRP-inducing stimuli have taken place [7–10]. Thus, tagging-and-capture is crucial to understand plasticity triggered by sequences of stimuli.

Neurophysiological experiments have established standardized protocols to induce the above described plasticity phenomena and tested many stimulus combinations, however, the space of possible combinations is infinite and cannot be mapped out by experiments completely. Therefore, mathematical and computational models are needed to extend our knowledge and extrapolate to new stimulation paradigms.

A plethora of models has been proposed since the discovery of tagging-and-capture. On the one hand, there is a large body of phenomenological models, which usually have an early and a late weight component [11–16]. These models consist of a few differential equations or states and are, therefore, well suited for network simulations. However, many of them lack biophysical interpretability and have to make strong assumptions. For example, to account for long-term stability of the late component, the latter is often assumed to be bistable (but see [15]). This gives rise to bimodal weight distributions, which is not in line with the experimentally measured unimodal weight distributions [17], and precludes LTP at already potentiated synapses, which severely limits memory capacity [18].

As the variables in the aforementioned models are typically not biophysically interpretable, their dynamics need to be inferred from existing experiments but do not necessarily extrapolate well to new experiments. This problem may be avoided if one considers actual biophysical quantities (e.g. concentrations of certain molecule species), whose dynamics (reaction kinetics) are known. For synaptic plasticity, such biophysically interpretable models typically take into account the detailed and complex signaling cascades that are, for example, triggered by calcium influx [19–22]. They are biologically much better interpretable, but their complexity usually precludes their usage in large-scale network simulations, which are necessary to tackle higher level brain functions. For such simulations, there is a need for light-weight models which still have a biophysical interpretation, which we aim to provide with the here proposed model.

To this end, we will consider only the dynamics of molecules that play a critical role in the processes of synaptic tagging-and-capture, focusing especially on the synaptic tag. Experiments have shown that the tag is likely not constituted by a single type of molecule [23], but rather relates to "a temporary structural state of the synapse" [6]. We will therefore consider the dynamics of the scaffolding protein actin as a major determining factor of the structure and follow the hypothesis that tagging can be modeled as a complex organizational state of actin and spine geometry [6, 24]. Actin is a globular protein which can form filaments that preferentially polymerize at one end and depolymerize at the other, which gives rise to a continuous treadmilling. When close to the membrane, this induces pushing forces and/or retrograde movement of the filament [25] which continuously alters the spine shape [26–29]. Additionally, multiple actin-binding proteins such as the branching protein complex ARP2/3 or the severing protein cofilin, organize the filaments into continuously growing and reorganizing, branched networks. Furthermore, crosslinking proteins such as drebrin,

actinin or CaMKIIβ [30, 31] can bind to the filaments, which slows down treadmilling and reorganization. Correspondingly, at least two populations of actin with different treadmilling speeds exist [32], which we refer to as the dynamic and the stable pool. Interestingly, the activity of the dynamic actin pool is localized to discrete polymerization foci [33], where an increased retrograde movement of filaments is observed. Following stimulation, the concentrations as well as the reaction rates of actin-binding rates change [31, 34]. While these changes are not long-lasting, they give rise to a rapid remodeling of spine geometry [28, 29, 35, 36], which may persist on the timescale of the synaptic tag [24].

To relate these geometrical dynamics to long-lasting plasticity of the synaptic transmission efficacy, we consider the dynamic of the postsynaptic density (PSD). The PSD is strongly correlated with the synaptic transmission efficacy (e.g., as measured by EPSPs [37]) through the number of AMPA receptors docked to the postsynaptic site. In particular it has been postulated that, depending on its size, the PSD provides a number of slots for AMPA receptors [6, 38]. Moreover, in the basal state, the PSD size is correlated with the spine volume [39]. Following the above described changes during a plasticity event, this correlation is disturbed, but it is reestablished on an timescale of minutes to hours [39, 40], consistent with the capture of PRPs and the decay of the transient changes in spine volume.

Here we present a model of synaptic tagging-and-capture that is based on actin and PSD dynamics in a biophysically realistic manner but at the same time lightweight enough to be used in large-scale network simulations. We show that this model reproduces the results of classical tagging-and-capture protocols as well as more sophisticated experiments involving multiple stimuli at the same synapse. We conclude that this model is suitable to predict the reaction of synapses to new stimulation protocols as well as to simulate the complex dynamics emerging in networks.

Results

Model for late-phase plasticity

Our novel model for late-phase plasticity is based on three quantities (see Fig. 1): (1) the amount of dynamic fast-treadmilling actin V_d, (2) the amount of cross-linked, stable actin V_s, and (3) the spine size corresponding to the current size of the postsynaptic density V_PSD (without active actin).

The temporal evolution of the actin pools is determined by (cf. Eqs. 1 & 2 in Methods):

$$\begin{aligned}
\frac{dV_\mathrm{d}}{dt} &= -k_\mathrm{b}V_\mathrm{d} + k_\mathrm{u}V_\mathrm{s} + k_\mathrm{growth}\cdot n_\mathrm{f}(t) - k_\mathrm{decay}\left[\frac{V_\mathrm{d}}{V_\mathrm{d}+V_\mathrm{s}} - c_0\right]_+ \left[V_\mathrm{d}+V_\mathrm{s}-V_\mathrm{PSD}\right]_+ , \\
\frac{dV_\mathrm{s}}{dt} &= +k_\mathrm{b}V_\mathrm{d} - k_\mathrm{u}V_\mathrm{s}.
\end{aligned}$$

Here, the first two terms on the right hand site cover transitions between the stable and the dynamic pool determined by crosslinker binding with rate k_b and unbinding with rate k_u. Experiments have shown that the polymerization of dynamic actin happens in distinct polymerization foci [33]. Thus, in our model, an additional growth term of the dynamic pool volume is proportional to the number such foci $n_\mathrm{f}(t)$. As such foci typically have a limited lifetime [27], the dynamics of this number is described as a stochastic birth-death process, where birth – the nucleation of new foci – happens with rate γ and their death with a rate μ.

Moreover, the dynamic pool also shrinks. If the sum of the actin-dependent volumes V_d and V_s is larger than the volume corresponding to the PSD size that is

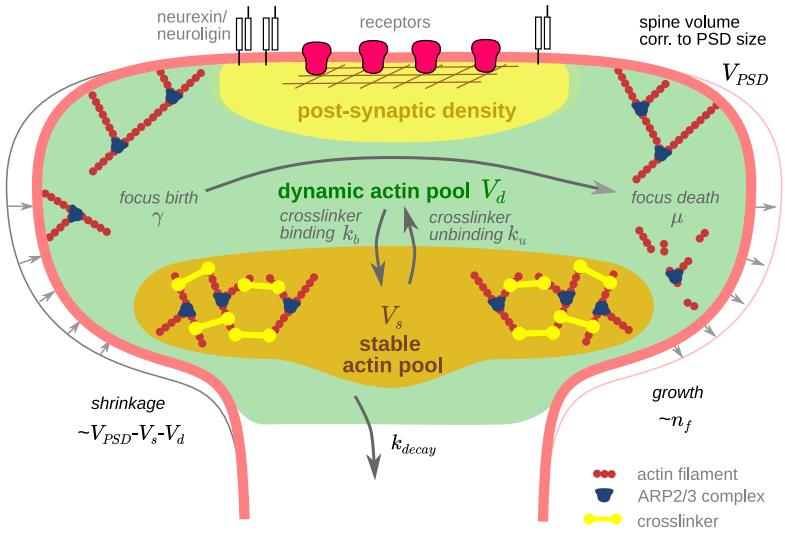

Fig 1. Sketch of the main quantities and processes in the novel late-phase plasticity model. Actin filaments are contained either in the dynamic or in the stable pool and can transit between these pools by binding and unbinding of crosslinkers.

expected without active actin, V_{PSD}, the membrane exerts counteracting forces. These forces hinder actin polymerization or push material out of the spine. Thus, the dynamic pool shrinkage is considered to be proportional to the difference between actin and PSD volume (as long as it is positive). If there is more dynamic actin, this effect will be stronger. Hence, the above described volume-dependent shrinkage is scaled by a factor that describes by how much the fraction of dynamic actin exceeds an offset concentration c_0.

Thus, taken together, there is no decay if the dynamic pool is below an offset concentration c_0 or if the volume of the actin pools is below the PSD-dependent volume. Otherwise, the dynamic pool will gradually reduce their difference with a rate k_{decay} and thereby reestablish the correlation between the total volume and PSD size [39, 41].

Finally, we model the temporal evolution of the PSD-dependent volume, which, given the above-described correlation, can serve as a proxy for the size of the PSD and ultimately also of the synaptic weight. Its dynamic is gated by the availability of PRPs, represented by $\phi(t)$ and it will only change if the actin volume is not in equilibrium with the PSD-dependent volume. The temporal evolution is therefore given by (cf. Eq. 3 in Methods):

$$\frac{dV_{\mathrm{PSD}}}{dt} = \phi(t) \cdot \left[V_{\mathrm{d}} + V_{\mathrm{s}} - V^*_{\mathrm{tot}}(V_{\mathrm{PSD}})\right] / \tau_{\mathrm{PSD}}.$$

Here, $V^*_{\mathrm{tot}}(V_{\mathrm{PSD}})$ is the total actin volume expected for the current PSD size under basal actin activity. It can be seen that, when PRP is available ($\phi_j = 1$), also the volume corresponding to the PSD size will evolve to reestablish the equilibrium with the actin volume. Hence, the difference between these two *acts as the synaptic tag* in our model. In contrast to other models, it does not depend on one but multiple dynamic variables of the system and, thus, represents a complex organizational state of the spine, which involves actin as well as spine and PSD geometry. We expect that this tag naturally decays due to the decay term of V_{d} trying to equilibrate actin and PSD. If PRPs are available, we expect that both V_{d} and V_{PSD} adapt concurrently until a new equilibrium is reached, which constitutes the late phase of synaptic plasticity.

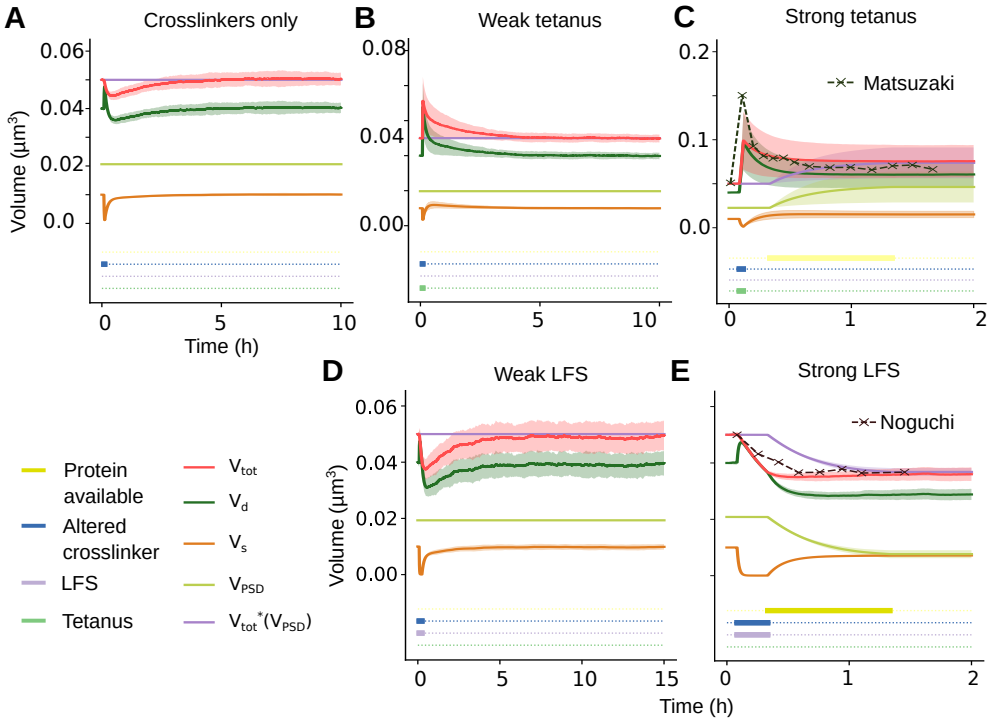

Fig 2. The novel late-phase model during LTP and LTD Time evolution of the dynamic and stable pool as well as V_{PSD} and derived quantities ($V_{\mathrm{tot}} = V_{\mathrm{d}} + V_{\mathrm{s}}$ and $V^*_{\mathrm{tot}}(V_{\mathrm{PSD}})$) over time under different conditions: (A) Plasticity-related alteration of crosslinker (un)binding (interval indicated by dark blue bar at bottom); (B) a weak tetanus (green bar) without PRP synthesis; (C) strong tetanus with PRP synthesis (yellow bar) (D) low frequency stimulation (purple bar) without PRP synthesis and (E) with PRP synthesis. Black dashed lines in panel C and E mark experimental results from the [41] and [42], which are matched by the model.

Testing the model for a single synapse and stimulus

To test these expectations, we initially assess the late-phase plasticity model on its own and induce synaptic plasticity by changing its parameters over time – that is, we switch these parameters to a new value at a given time relative to the plasticity-inducing stimulus and revert them to their original value after a defined time interval (see Methods and bottom of panels in Figs. 2-5 for the respective time intervals). In particular two sets of parameters are changed: Firstly, it is known that during LTP crosslinkers rapidly unbind from the actin filaments, filaments are severed and new actin foci emerge [31]. Similarly, also during LTD, crosslinker dynamics are altered [43, 44]. In our model, this is reflected by a change in crosslinker binding and unbinding rates. Secondly, the influx of calcium during both LTD and LTP can trigger multiple signaling chains, which regulate, for example, the actin severing protein cofilin [45]. This can lead to increased severing and thus death of actin polymerization foci, but also to a large concentration of free actin monomers and nucleation of new filaments. Thus, in the model, we vary birth and death rates of actin foci accordingly.

In order to assess the influence of individual rate changes, we first tested what would happen if the crosslinker binding and unbinding rates are transiently altered (Fig. 2A). As expected, we found that this leads to a rapid transfer of actin from stable (ocher curve) to dynamic pool (dark green curve) and the subsequent slow

restoration of the stable pool to its stationary value, whereas the total volume of the actin pool only shortly dips and remains approximately at the same level (pink curve). An increase in the total volume is elicited, when the birth rate of new foci is increased in parallel (Fig. 2B), which corresponds to a weak tetanization in experiments. Here, we first observe an even stronger increase of the dynamic pool, which is transferred to a transient increase of the stable pool above its stationary level after the crosslinkers return to their normal rates. However, without PRP synthesis all quantities ultimately return to their initial (stationary) values. This is because the decay term in V_{d} drives the total volume of actin towards the volume determined by the PSD size V_{PSD}. However, if PRP synthesis is switched on (as during strong tetanization), V_{PSD} and, thus, V^*_{tot} become dynamic and adapt to the perturbed total actin volume (Fig. 2C, violet and ocher). As soon as V^*_{tot} reaches the total actin volume, no further change happens. This is due to the fact that, by construction, $V^*_{\mathrm{tot}} = V_{\mathrm{d}} + V_{\mathrm{s}}$ is a line attractor when PRP synthesis is enabled (see Appendix). The model parameters used throughout the manuscript were chosen such that the time course of V_{tot} resembled the relative volume changes from LTP-inducing glutamate uncaging experiments ([41], black dashed line in Fig. 2C).

Similar to the workings of LTP, our model can also account for LTD. Here we assume that crosslinkers unbind similarly to the LTP situation, but the birth rate of new foci is decreased. This leads to a smaller increase in the dynamic pool volume upon stimulation and a dip in the total actin volume (Fig. 2D-E). When no PRP synthesis occurs, the total volume starts to increase again as soon as the stimulus ends and the birth rate of new foci is restored until the pre-stimulus level is reached (Fig. 2D). When PRP synthesis is enabled, this negative perturbation is translated to a negative change in V_{PSD} (Fig. 2E). Here again, we adjusted our model to match the time course of spine volumes after a low-frequency stimulation observed in experiments (dashed line, [42]).

Integration with calcium-based early-phase plasticity and synthesis of plasticity-related products (PRPs)

As a next step towards a full model of synaptic tagging-and-capture, we integrated our novel late-phase plasticity model with a calcium-based early-phase model (cf. [46]) and a PRP synthesis model (cf. [11]), as it was done with simpler models in earlier studies [14, 15]. The integrated model comprises a weight component for early-phase plasticity that undergoes LTD when the calcium amount exceeds a threshold value θ_{d}, and LTP when calcium exceeds an even higher threshold θ_{p}. Otherwise the early weight decays towards its baseline value zero. PRP synthesis takes place when the deviations from the baseline, summed over all synapses of a neuron (referred to as "signal triggering PRP synthesis", SPS – red curves in bottom panels in Fig. 3) exceeds a threshold θ_{ϕ} (cf. Eq.6).

For the current study, the calcium signal at the synapse is also used to determine the crosslinker activity and the dynamics of actin foci: When calcium is above the LTD threshold θ_{d}, the signaling chain for depression is activated. We here chose calcineurin (CaN, [45]) as a representative of this signaling chain and include a calcineurin signal that activates when calcium is above that threshold. The signal remains activated for a certain time afterward and as long as it is active, the above described effects of the LFS on the late-phase model are applied. Similarly, for tetanic stimulation and LTP, we model a CaMKII signal that activates when calcium is above a higher threshold θ_{CaMKII} and triggers the proposed effects of tetanic stimulation on the late-phase model.

In our full-integrated model, we consider the PSD-dependent volume V_{PSD} as a

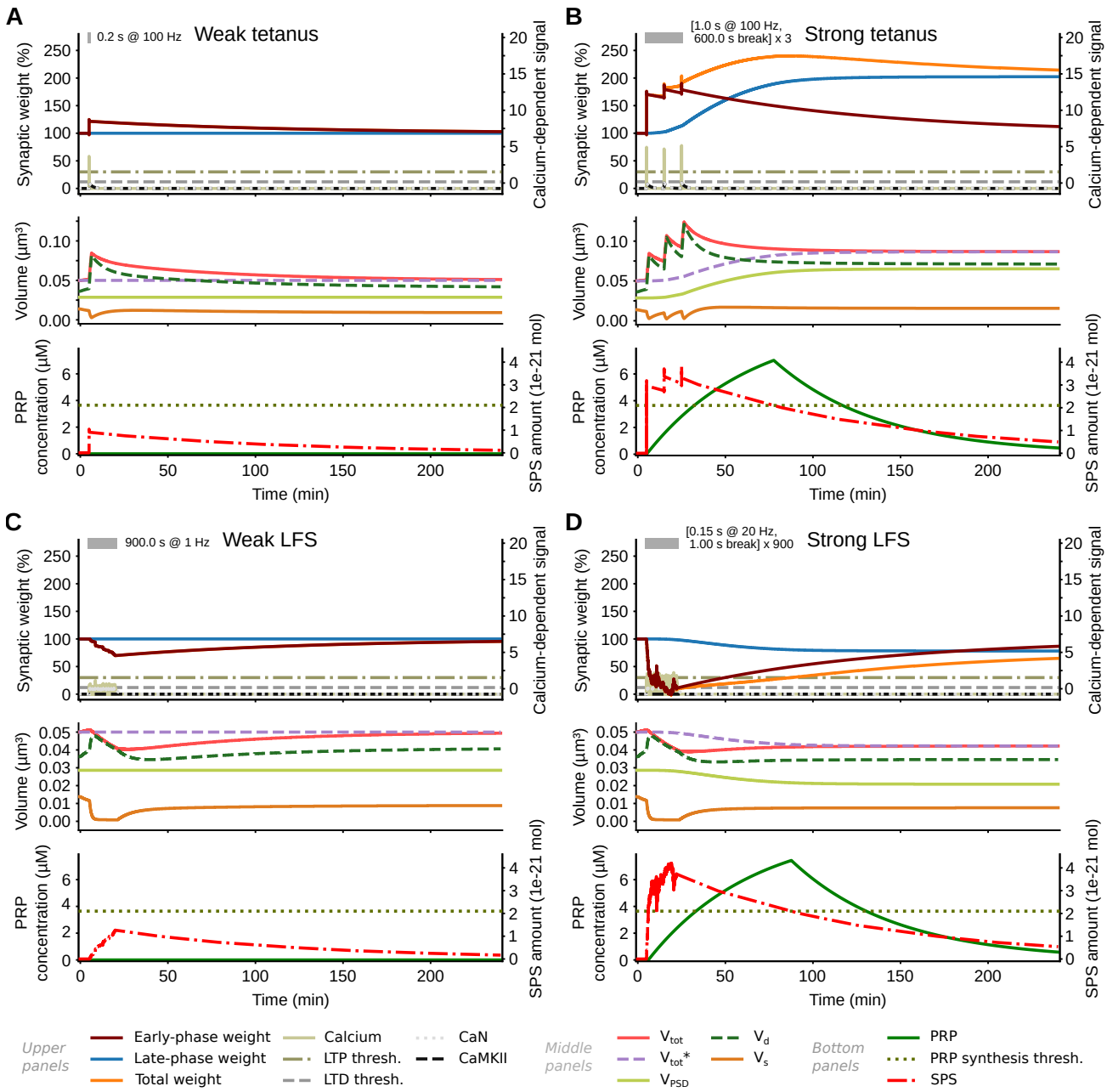

Fig 3. Temporal evolution of synaptic weights and all relevant signals in the full-integrated, calcium-based model under different stimulation protocols: (A) weak tetanization leads to e-LTP, (B) strong tetanization induces l-LTP, (C) weak low-frequency stimulation induces e-LTD, and (D) strong low-frequency stimulation yields l-LTD.
Upper panels: Early-phase (brown, shifted for visualization purposes), late-phase (blue), and total weight (orange) of the individual synapse as well as calcium-dependent signals (calcium amount, CaN activity, and CaMKII activity, in normalized units). LTD and LTP thresholds are shown by dashed and dash-dot horizontal lines; CaMKII threshold $\theta_{\mathrm{CaMKII}} = 5$ not shown. Gray bar at the top: information on the time point, duration, and structure of the stimulation.
Middle panels: Quantities of late-phase plasticity of the individual synapse (dynamic pool: dark green dashed, stable pool: ocher, total volume: pink, PSD volume: light green, V^*_{tot}: purple compare Fig. 2).
Bottom panels: Quantities of neuron-wide processes – concentration of available PRP (dark green) and amount of the signal triggering PRP synthesis (SPS, red).

proxy for the late-phase weight z. In particular, we calculate z as a linear function of V_{PSD} (cf. Eq. 8). This late-phase weight is added to the early-phase weight h to yield the total weight of the synapse as $w(t) = h(t) + z(t)$.

Using this model in a small circuit of leaky integrate-and-fire neurons, we could induce plasticity via a presynaptic spiking activity resembling the stimulation used in classical tagging-and-capture experiments (cf. [47]; see Methods), similar as for the simple switching of the rate parameters in our late-phase-only model earlier.

During a weak tetanus (Fig. 3A), calcium rises above the thresholds for early LTP and CaMKII activation. This leads to similar actin dynamics as in Figure 2B. The increase of the early weights is however not large enough for the SPS signal to cross the threshold for PRP synthesis (3A bottom), such that all quantities eventually decay to their initial values. The strong tetanus (Fig.3B, which consists of three prolonged stimulation intervals of the same high frequency, leads to more early LTP and thereby triggers PRP synthesis. Also, the total amount of actin is summing up changes from multiple stimulations, which are then translated into an increase of V_{PSD} (which serves as a proxy for the late-phase weight, as mentioned before).

For low-frequency stimulation (Fig. 3C and D), we obtain calcium levels above the depression threshold but below the potentiation and CaMKII thresholds. Thus, actin nucleation is decreased and the overall actin volume decays. For strong low-frequency stimulation, however, enough early-phase plasticity is expressed to trigger PRP synthesis, such that V_{PSD}, and thus the total weight, decreases.

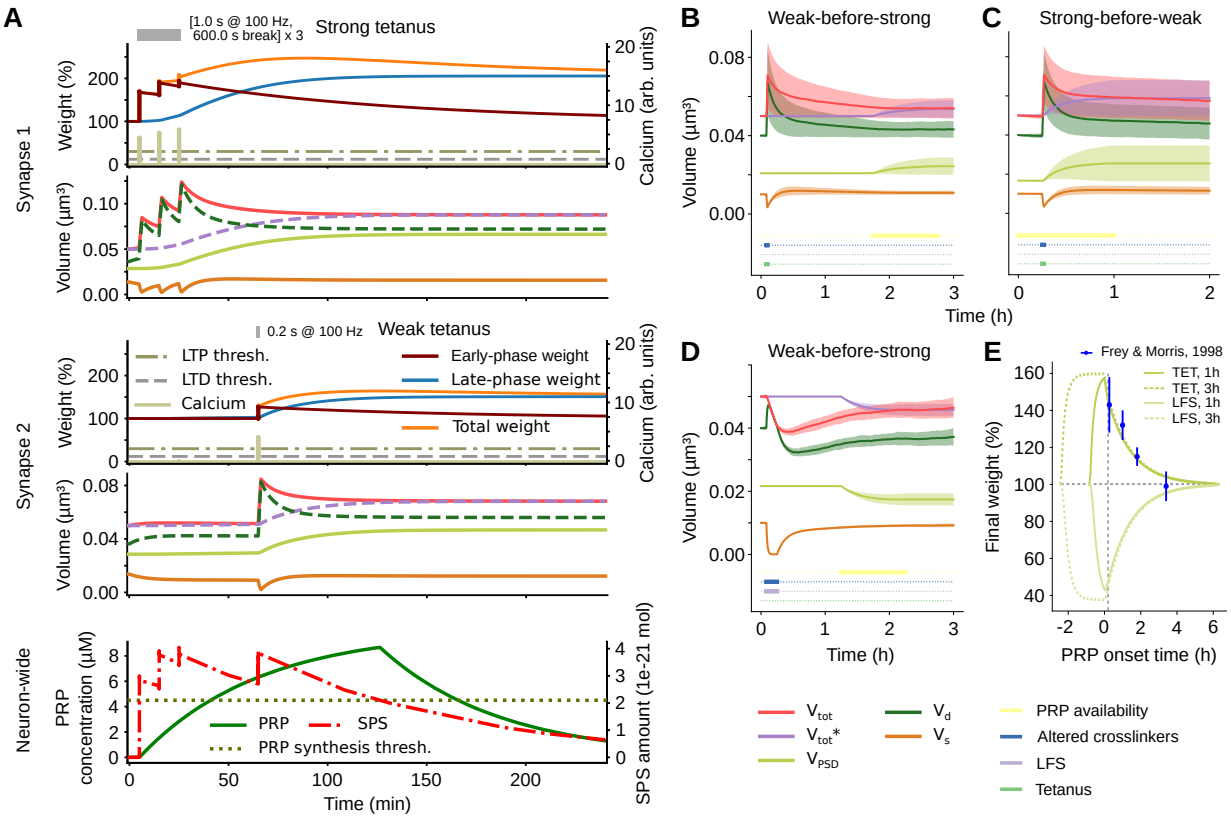

Fig 4. Heterosynaptic tagging-and-capture (A) Example of a strong-before-weak tetanization protocol in the full-integrated model (strong tetanus via first synapse starting at 300 s, weak tetanus via second synapse starting at 3900 s, cf. Fig. 3); (B) weak-before-strong tetanization in the late-phase only model; (C) same for strong-before-weak tetanization; (D) same for weak-before-strong low-frequency stimulation. (E) Final values of V_{tot} and V_{PSD} in the late-phase-only model after weak tetanus (vivid color) and LFS (pale color), under systematic variation of the onset of PRP availability due to a strong stimulus. Strongest plasticity occurs when PRP is available at the time of the weak stimulus. For PRP availability before the stimulus, the duration of PRP availability (1 h solid line, 3 h dashed line) determines the maximal time difference between strong and weak stimuli. The dashed vertical line marks the PRP availability used for the reduced model in the rest of the study. Experimental results [48] are shown for comparison (data points in blue).

Heterosynaptic tagging-and-capture

As a next step we investigated the behavior of our model under tagging-and-capture protocols for heterosynaptic plasticity. Here, weak and strong stimuli are applied with a time delay at different synapses of the same neuron. The weak stimulus elicits early-phase plasticity but does not trigger PRP synthesis and thus no late-phase plasticity. However, it leaves a synaptic tag at the stimulated synapse. Complementary to this, the strong stimulus at another synapse elicits PRP synthesis, which can be used by the tag at the weakly stimulated synapse to produce late-phase plasticity.

In order to test this, we simulated a situation where the strong stimulation arrives before the weak stimulation in our full-integrated model, finding that the weak stimulus, which by itself could cause no changes of the late-phase weight (Fig. 3A) now indeed leads to a persistent increase in the PSD volume, and, thus, the late-phase-weight (Fig. 4A, panels for synapse 2).

Knowing that heterosynaptic tagging works in the full-integrated model, we systematically analyzed its determinants using again the late-phase-only plasticity model. We focused on the emergence of late-phase plasticity at the weakly stimulated synapse, considering that PRP synthesis is triggered by a strong stimulus at another synapse at a time before (strong-before-weak protocol, Fig. 4C) and after the weak plasticity event (weak-before-strong protocol, Fig. 4B, D). When the strong stimulus arrives after a weak tetanus (Fig. 4B), PRPs become available later than for normal LTP. At this time the total volume of the actin pools has decayed towards its stationary value, and hence the adaptation of V_{PSD} that is needed to match this volume becomes smaller. As a consequence, we expect a decreased magnitude of late-phase LTP for a weak-before-strong tetanic protocol. Similarly, also for a weak LFS arriving before a strong stimulus (Fig. 4D), we observe a decreased magnitude of late-phase LTD. In contrast, for the strong-before weak protocol, PRP is available at the weakly stimulated synapse already at the time of stimulation such that the magnitude of late-phase changes is larger (Fig. 4C). Yet, in both cases the final PSD volume is set apart from its initial level, indicating that late-phase plasticity has taken place.

We then systematically varied the onset time of PRP availability with the late-phase-only model, finding that the maximal effect of both LTP and LTD is achieved if PRP synthesis starts together with the weak stimulus (Fig. 4E). If the strong stimulus occurs before the weak one, PRP needs to be available until the stimulus-induced imbalance of the actin volumes and the PSD volume at the weakly stimulated synapses are fully equilibrated. Otherwise, the PSD dynamic will stop early and the rest of the equilibration is only achieved by dynamic pool changes. Hence, the duration of PRP availability determines how long before the weak stimulus the strong one can be started to yield maximal late-phase plasticity. If PRP is available for one hour, maximal plasticity is achieved when the PRP synthesis starts immediately at the weak stimulus (Fig. 4E, solid lines). If PRP availability is prolonged to 3 hours (Fig. 4E, dashed lines), PRP synthesis could start up to 1.5 hours before the stimulus and still lead to maximal changes.

On the other hand, if PRP synthesis starts after the stimulus (weak-before-strong), we observe the same gradual decay of the late-phase plasticity for both cases. Here, initially only the dynamic pool volume adapts to the PSD and decreases the imbalance. Consequently, less change of the PSD is needed to match the volume, once the PSD dynamic is turned on.

We conclude that, in our model, the imbalance between PSD volume and actin volumes retains the memory of the plasticity event for a certain period of time and, therefore, can serve as the synaptic tag. The precise lifetime of the tag can be assessed through the presented weak-before-strong experiments. We selected the parameter

values here such that the time course matches that found in electrophysiological experiments (Fig. 4E blue data points based on [48]).

Two subsequent stimuli at the same synapse

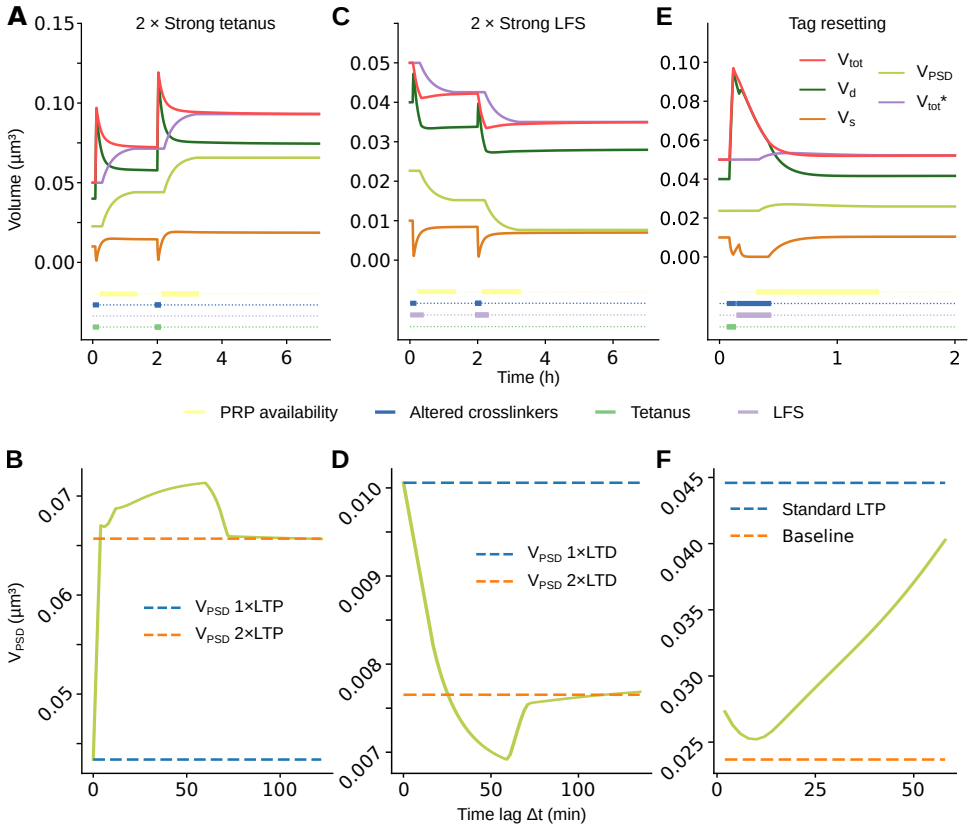

Fig 5. Effect of two stimuli at one synapse and their timing (A) The effect of two strong tetanus stimuli stacks linearly when they are sufficiently separated (here 2 hours). (B) Dependence of plastic changes (i.e. the final value of V_{PSD}) on temporal lag between strong tetanus stimuli. (C) The effect of two spaced strong LFS stacks linearly as well. (D) Dependence of plastic changes on temporal lag between strong LFS stimuli. (E) Tag resetting: a strong LFS 5 min after a strong tetanus stimulus blocks the late-phase LTP effect. (F) Systematic analysis of the plasticity effect depending on LTP-LTD temporal lag, which reveals that tag resetting only works within a short time window after tag setting.

LTP and LTD spacing

As a last step, we evaluate the reaction of our model to multiple plasticity-inducing stimuli. To reduce complexity, we restrain our analysis to the late-phase-only plasticity model with switching rates. In particular, we tested whether the lasting late-phase changes from multiple LTP- or LTD-inducing stimuli stack linearly and how the timing between the events influences this. For this, we first applied two high-frequency (tetanic) stimuli separated by a defined time interval (e.g., 2h in Fig.5)

and evaluated the total volume as well as the PSD size after all quantities have equilibrated. We compare these with the result of a single LTP event (blue dashed line in Fig.5B) and of two consecutive but sufficiently separated LTP events (orange dashed line). We observe that, for inter-stimulus intervals of a few minutes, the resulting volume and PSD size are smaller than for two independent events (sub-linear stacking), indicating an occlusion of LTP (see [49] for experimental evidence of this. After that, however, we observe a super-linear stacking of the LTP events for inter-stimulus intervals of up to 75 minutes. After this interval, the PRP availability of the first stimulus has vanished and there is no influence on the second stimulus such that the results match those of two far separated LTP-events (linear stacking).

We further assessed how the temporal spacing between two low-frequency stimuli influences LTD. Similar as for LTP, we observe weaker LTD (sub-linear stacking) for inter-stimulus-intervals up to 45 minutes and stronger LTD (super-linear stacking) in a time window from 45 to 75 minutes after the first stimulus (Fig.5C-D).

Taken together our model predicts that around an hour after a stimulus, a repeated stimulus causes a stronger plasticity effect. This may relate to psychological effects such as spaced learning [50].

Tag resetting

Finally, we tested how consecutive tetanic and low-frequency stimuli would influence the weights in our model. We find that for a sufficiently small inter-stimulus interval (e.g., 5 minutes in Fig. 5E), there will be no late-phase plasticity, indicating that the tags from LTP and LTD events cancel each other out. However, for longer inter-stimulus intervals we observe that late-phase potentiation re-emerges (Fig. 5F), which is consistent with spine volume data on tag resetting (no LTP at 15 min but LTP at 30 min, see [51]). Thus, we conclude that our model can indeed reproduce the late-phase plasticity produced by two interacting stimuli.

Discussion

In summary, we have derived a biophysically interpretable reaction rate model for the key players in structural and functional synaptic plasticity that can reproduce not only experiments on late-phase LTD and LTP but also on heterosynaptic synaptic tagging-and-capture experiments and the interaction of multiple, temporally adjacent stimuli according to the tagging-and-capture framework. We would like to point out that this is an important feature, as most phenomenological synaptic plasticity models do not include interaction of consecutive stimuli on a timescale of minutes [52].

Such an integration might however be very beneficial for neural systems. On the one hand, the adaptation of synaptic weights needs energy and it is likely that the brain would employ plasticity mechanisms that are energy efficient [53]. Recent research has shown that this energy-efficiency can be achieved by having a fast plasticity mechanism with small energy cost that integrates over a few stimuli and a slow plasticity mechanism with larger energy cost that adapts the synaptic weights only if needed [54]. In our model the fast process would be implemented by the structural changes that induce a continuous synaptic tag which is manifested by the imbalance between actin volumes and PSD in our model. Through multiple stimuli, this imbalance can be enlarged or shrinked and even pushed to the opposite sign. This process is likely energy efficient as it is implemented by slight tweaks of the local actin dynamics. The slow plasticity mechanism given by the PSD adaptation then transfers this tag into actual functional changes, but can be considered to be less energy

efficient as it involves *de novo* protein synthesis and/or transport of molecules (such as proteins or mRNA) from the soma.

Two-phase plasticity mechanisms have also been proposed to enhance storage capacity in neural networks [55–58]. Furthermore, in contrast to earlier plasticity models that often assume bistable late-phase weights, a line attractor, as we consider here, may improve storage capacity by allowing for a continuous range of synaptic weights. For example, it can facilitate the storing of overlapping ensembles of neurons [59], where simpler bistable models would suffer from interference due to their inability to add up multiple increases in synaptic weight (also see our investigations in Fig.5). In theory [18], the line attractor can enable networks to store memory representations with an optimized set of weights, mitigating catastrophic forgetting and improving storage capacity.

The implementation of our full-integrated model with the Arbor simulator (see Methods) enables to seamlessly deploy the model in network simulations with single- or multi-compartment neurons (cf. [60]). In particular, our own previous network models [15, 59, 61], which have considered a simpler model of synaptic tagging-and-capture combined with the same calcium-based model of early-phase plasticity that we used here, may thus easily be extended to account for the biophysically more realistic actin-based formulation that we have presented here. This may provide more detailed insights into the impact of multiple stacked learning stimuli as mentioned above (cf. [59]), the impact of the timing of PRP synthesis at the network level (possibly depending on neuromodulators, cf. [61]), as well as the priming of memory representations on timescales of the synaptic tag [59]. Furthermore, with few adjustments, also other network models featuring synaptic tagging-and-capture ([13, 57, 62], see [63] for a review) may be improved by adding our proposed biophysical late-phase mechanisms.

Methods

Actin-based model of tagging-and-capture

Long-lasting synaptic alterations due to synaptic tagging-and-capture are known to depend on dynamic actin [70, 71]. Changes in actin dynamics affect spine geometry, which is followed by alterations of post-synaptic density [39]. These, in turn, correlate with the number of bound AMPA receptors and, thus, the synaptic weight. Following this reasoning, we model tagging-and-capture based on the amount of dynamic, fast-treadmilling actin V_d (size of the dynamic pool), the amount of cross-linked, stable actin V_s (size of the stable pool), and the spine size corresponding to the current size of the postsynaptic density V_PSD. The dynamics of the system are given by:

$$\begin{aligned}\frac{dV_\mathrm{d}}{dt} &= -k_\mathrm{b}(t)V_\mathrm{d} + k_\mathrm{u}(t)V_\mathrm{s} + k_\mathrm{growth}n_\mathrm{f}(t), \\ &\quad -k_\mathrm{decay}\left[\frac{V_\mathrm{d}}{V_\mathrm{d}+V_\mathrm{s}} - c_0\right]_+ \left[V_\mathrm{d}+V_\mathrm{s}-V_\mathrm{PSD}\right]_+, \qquad (1)\\ \frac{dV_\mathrm{s}}{dt} &= +k_\mathrm{b}(t)V_\mathrm{d} - k_\mathrm{u}(t)V_\mathrm{s}, \qquad (2)\\ \frac{dV_\mathrm{PSD}}{dt} &= \phi(t)\cdot\left(V_\mathrm{d}+V_\mathrm{s}-V^*_\mathrm{tot}(V_\mathrm{PSD})\right)/\tau_\mathrm{PSD}. \qquad (3)\end{aligned}$$

Here, k_b and k_u are the crosslinker binding and unbinding rates, k_growth and k_decay the rates for dynamic pool growth and shrinkage, $\phi(t)$ the PRP availability, τ_PSD the PSD reorganization timescale, $[x]_+ = (x+|x|)/2$ the rectification function, and n_f the number of active polymerization foci. More detailed simulations of the actin network

Param.	Value	Description	Reference
k_{growth}	$135 \cdot 10^{-6}$ s^{-1} µm^3	growth rate of the dynamic actin pool	
k_{decay}	1/380 s^{-1}	decay rate of the dynamic actin pool	[5]
τ_{PSD}	380/0.255 s	adaptation rate of the PSD (with PRPs)	[39]
c_0	0.725	basal fraction of dynamic actin	
τ_c	0.0488 s	calcium timescale	[14, 15, 46]
c_{pre}	1	calcium increase per presynaptic spike	[14, 15, 46]
c_{post}	0.2758	calcium increase per presynaptic spike	[14, 15, 46]
t_{cad}	0.0188 s	delay of calcium increase with respect to presynaptic spike	[14, 15, 46]
θ_{p}	3.0	potentiation threshold	[14, 15]
θ_{d}	1.2	depression threshold	[14, 15]
θ_{CaMKII}	5.0	threshold for CaMKII activity	
γ_{p}	1645.6	early-phase potentiation rate	[46]
γ_{d}	313.1	early-phase depression rate	[46]
τ_h	688.4 s	early-phase weight timescale	[46]
σ_{wn}	2.90436 mV	scaling factor for fluctuations of early-phase plasticity	[46, 59]
τ_{CaMKII}	120 s	timescale of CaMKII deactivation	[64, 65]
τ_{CaN}	120 s	timescale of CaN deactivation	[65]
θ_ϕ	2.10037 mV	PRP synthesis threshold	[14]
τ_ϕ	3600 s	PRP timescale	[11, 14]
α_ϕ	1	PRP synthesis rate	[11, 14]
c_w	4.20075 mV	constant determining the initial value and dynamics of the total synaptic weight	[46, 59]
c_{late}	0.8	late-phase fraction of the total weight	[14, 15]
τ_{mem}	10 ms	membrane time constant	[52, 66]
τ_{syn}	5 ms	synaptic time constant	[52, 66, 67]
t_{axd}	3 ms	axonal transmission delay	[66, 68]
t_{ref}	2 ms	absolute refractory time	[52, 69]
V^{rev}	−65 mV	reversal (equilibrium) voltage	[52]
V^{th}	−55 mV	threshold voltage for firing	[52]
V^{reset}	−70 mV	reset voltage	[52]

Table 1. Parameter values and sources for both the late-phase model and the other parts of the full-integrated model.

Stimulus	Birth γ	Death μ	$\langle n_{\text{f}} \rangle$	k_{b}	k_{u}	Interval	PRPs available
Basal	0.02 s^{-1}	0.5 s^{-1}	0.04	1/2480 s^{-1}	1/620 s^{-1}	-	-
Weak tetanus	0.45 s^{-1}	0.5 s^{-1}	3.12	1/55000 s^{-1}	1/55 s^{-1}	[0 s, 60 s]	-
Strong tetanus	0.45 s^{-1}	0.5 s^{-1}	3.12	1/55000 s^{-1}	1/55 s^{-1}	[0 s, 120 s]	[900 s, 4300 s]
Weak LFS	0.0 s^{-1}	0.05 s^{-1}	0.0	1/55000 s^{-1}	1/55 s^{-1}	[0 s, 600 s]	-
Strong LFS	0.0 s^{-1}	0.05 s^{-1}	0.0	1/55000 s^{-1}	1/55 s^{-1}	[0 s, 900 s]	[900 s, 4300 s]

Table 2. Time-dependent changes of the crosslinker and actin foci dynamics after stimulation. The reported $\langle n_{\text{f}} \rangle$ is used in simulations, where the birth-death-process is replaced by a constant n_{f}-value and tuned to yield comparable results as the stochastic simulations.

suggest that n_f fluctuates heavily because new foci continuously emerge while old foci die out [27, 28]. To approximate this, we here determine n_f by a birth-death process, with a birth rate γ and a death rate μ.

While

$$V_\mathrm{tot} = V_\mathrm{d} + V_\mathrm{s}$$

represents the total volume of the spine with active actin dynamics, expected for the current PSD size,

$$V^*_\mathrm{tot}(V_\mathrm{PSD}) = V_\mathrm{PSD} + \frac{k_\mathrm{growth} \cdot \langle n_\mathrm{f} \rangle}{k_\mathrm{decay}} \left(\frac{k_\mathrm{u}}{k_\mathrm{b} + k_\mathrm{u}} - c_0 \right)^{-1}$$

is the steady-state volume set such that the PSD does not change in equilibrium with actin (see Appendix), where $\langle . \rangle$ denotes the temporal average. Note, in the absence of dynamic actin foci ($n_\mathrm{f} = 0$), V^*_tot equals V_PSD.

Time-dependent parameters during LTP and LTD induction

During plasticity the crosslinker binding and unbinding as well as the birth and death rate of actin foci are altered as described in the following. All constant parameters are reported in Table 1.

After stimulation, the actin cytoskeleton can undergo highly dynamic changes as actin-binding proteins change their concentrations and binding rates. For example, cofilin gets activated after an LTP-inducing stimulus, which leads to a massive severing and, in turn, produces an abundance of free actin and creates new foci [31, 34]. Moreover, crosslinkers unbind from the filaments [30, 31, 34]. Although not so well documented, the latter may also occur for LTD [43, 44].

In order to study our model (Eqs. 1–3) during plasticity, we first implement time-dependent parameters in the form of step functions, which switch their value at given time-points after a putative LTP or LTD event. We use the following alterations, which are summarized in Table 2:

Weak and strong stimulations In general, strong stimuli induce late-phase plasticity, while weak stimuli only induce early-phase effects. Thus, for weak stimuli, the duration of the rate alterations is smaller and $\phi(t)$ is kept at zero throughout the experiment. In contrast, for strong stimuli, we set the PRP availability to $\phi \equiv 1$ for 60 minutes starting 15 minutes after the stimulus (if not stated otherwise; also cf. PSD changes in [39]).

Tetanic stimulation Tetanic, i.e., high-frequency stimulation can induce LTP. Accordingly, immediately after a tetanic stimulation event, the birth rate of the stochastic process is significantly increased and the death rate is decreased for the typical duration of a tetanization protocol (60 s/120 s for weak and strong, respectively). This corresponds to an increase of cofilin in the spine, which has experimentally been observed in the early phase of LTP [34]. Also, within the first minutes of LTP, crosslinkers unbind from actin and/or leave the spine [34, 43, 72]. Therefore, in the model, the crosslinker binding and unbinding rates k_b and k_u rates are increased to allow faster exchange between the two pools, shifting their balance towards unbinding, which results in a smaller stable actin pool.

Low frequency stimulation (LFS) LFS can give rise to LTD. Accordingly, in our model, we set the birth rate of actin foci to zero and increase the death rate for the duration of the stimulus (600 s/900 s). The crosslinker binding rates are subject to

the same transformation as in LTP, but in this case, the duration of the effect is prolonged to remain for the duration of the LTD stimulus.

Parameter estimation

To find parameters that match experimental characterizations of synapses, we used three different datasets: (1) volume time courses after glutamate uncaging inducing LTP [41] (2) and LTD [42], as well as (3) electrophysiological data from the weak-before-strong protocol [48]. For each datapoint, we calculated the squared error of the relative volume changes, normalized by the size of the experimentally observed volume change. We weighted the errors of the 3 datasets with $w = (1, 2, 10)^T$ to account for the imbalance between the number of data points, and calculated the sum over all these weighted normalized errors. We then minimized this error. For numerical stability, we used the inverse of the rates as well as the product of covariant parameters as free parameters (with their bounds in brackets):

- the timescale for crosslinker unbinding $1/k_{\mathrm{u}} \in [300\,\mathrm{s}, 1500\,\mathrm{s}]$
- the dynamic pool decay timescale $1/k_{\mathrm{decay}} = 240\,\mathrm{s}$ (varied in step 2 only, see below)
- the ratio between dynamic pool decay and PSD adaptation timescales $\in [0.05, 0.5]$
- the product (mean) number of active foci and the growth rate k_{growth}, $\in [4 \cdot 10^{-5} \cdot V^*_{\mathrm{tot}}(t = 0),\ 2 \cdot 10^{-4} \cdot V^*_{\mathrm{tot}}(t = 0)]$
- same product during LTP $\in [6 \cdot 10^{-3} \cdot V^*_{\mathrm{tot}}(t = 0),\ 2 \cdot 10^{-2} \cdot V^*_{\mathrm{tot}}(t = 0)]$
- the offset fraction of the dynamic pool $c_0 \in [0.7, 0.75]$

For minimization, we used a two-step procedure:

1) **Bayesian optimization:** Using the Bayesian Optimization package [73], we scanned for local optima in the above specified parameter regime by using 200 initial samples and 50 samples from the Optimizer

2) **Minimizer** The resulting best parameter set was then passed to an gradient decent optimizer (Nelder-Mead from scipy optimize) in order to reach the local minimum. Hereby, the parameter changes were bounded within 10% of the initial value. Throughout the process, rates were rounded to multiples of 5 s.

After that, other parameters were derived as follows: The ratio between binding and unbinding timescales was set to 1/4 to obtain 20% stable pool fraction [32].

Integration with calcium-based early-phase plasticity and PRP synthesis

In order to study its interaction in neural circuits, we coupled our model of late-phase plasticity to established models for neuronal activity, calcium-based early-phase plasticity, and PRP synthesis (cf. [14, 15, 63]). Large parts of the formulation below thus follow previous descriptions [15, 59]. Note that as compared to [15, 59], we use here a transformed formulation of the early- and late-phase dynamics where the baseline of the early-phase weights is $h(t = 0) = 0$ and the baseline of the late-phase weights is $z(t = 0) = c_w$. This formulation is equivalent to the one in the previous studies, but may be easier to interpret from a biological perspective (the baseline of the total weight is here set by the stable late-phase weight).

Calcium

LTP and LTD are known to rely on calcium signaling both on a morphological and functional level [41, 46, 74]. Therefore, in our model, the calcium level $c_{ji}(t)$ at the post-synaptic site of synapse from neuron i to neuron j is the major factor to induce plasticity. Following [46], the calcium level is increased by c_{pre} for every presynaptic spike at time t^n and by c_{post} for every postsynaptic spike at time t^m, and it evolves according to:

$$\frac{dc_{ji}(t)}{dt} = -\frac{c_{ji}(t)}{\tau_c} + c_{\text{pre}} \sum_{t' \in S(j)} \delta(t - t' - t_{\text{cad}}) + c_{\text{post}} \sum_{t' \in S(i)} \delta(t - t'), \tag{4}$$

where $S(i)$ and $S(j)$ mark the set of spike times of neurons i and j, respectively, $\delta(\cdot)$ is the Dirac delta distribution, τ_c is a time constant, and t_{cad} accounts for the delayed increase of calcium for presynaptic spikes (due to axonal conduction delays).

Early-phase plasticity

Early phase-plasticity is based on altered receptor trafficking driven by the calcium concentration in the postsynaptic spine [38, 75]. We model this by an early-phase weight $h(t)$ following a calcium-based plasticity rule with two thresholds for depression and potentiation, respectively [14, 15, 46]. The dynamics are described by:

$$\begin{aligned}\tau_h \frac{dh_{ji}(t)}{dt} = &-0.1 \cdot h_{ji}(t) + \gamma_{\text{p}} \cdot (10\,\text{mV} - (h_{ji}(t) + c_w)) \cdot \Theta(c_{ji}(t) - \theta_{\text{p}}) \\ &-\gamma_{\text{d}} \cdot (h_{ji}(t) + c_w) \cdot \Theta(c_{ji}(t) - \theta_{\text{d}}) + \xi(t),\end{aligned} \tag{5}$$

where $\Theta(\cdot)$ is the Heaviside step function, c_w is a constant that determines the initial value and dynamics of the total synaptic weight, τ_h is the calcium decay time constant, $c_{ji}(t)$ is the calcium concentration at the postsynaptic site, and $\xi(t)$ is a noise term (see below).

The first term on the right-hand side describes the relaxation of the early-phase weight to zero, the second term describes the induction of early-phase LTP with rate γ_{p} (requiring that the calcium amount is above the threshold θ_{p}), and the third term describes the induction of early-phase LTD with rate γ_{d} (requiring that the calcium amount is above the threshold θ_{d}). As the latter two terms are multiplied by $(h_{ji}(t) + c_w)$ and $(10\,\text{mV} - (h_{ji}(t) + c_w))$, the early weight is soft-bounded to an interval $[-c_w, 10\,\text{mV} - c_w]$. Finally, the noise term depends on Gaussian white noise $\Gamma(t)$ with mean zero and variance $1/dt$, and is given by (cf. [46])

$$\xi(t) = \sqrt{\Theta\left(c_{ji}(t) - \theta_{\text{p}}\right) + \Theta\left(c_{ji}(t) - \theta_{\text{d}}\right)} \cdot \sqrt{\tau_h} \cdot \sigma_{\text{wn}} \cdot \Gamma(t),$$

with the factor σ_{wn} scaling its standard deviation.

Synthesis of PRPs

Synthesis of plasticity-related products (PRPs), in particular, of proteins, has been found to occur in the soma as well as locally in dendrites. Thus, there is evidence for both global and local PRP dynamics [76–80]. In our full-integrated model, we describe PRP dynamics as a neuron-wide process of synthesis and decay. To determine the onset of PRP synthesis, we define a "signal triggering PRP synthesis" (SPS) as the

absolute deviation of the early-phase weights from their stationary value 0 summed over all incoming synapses (cf. [14]):

$$\mathrm{SPS}_j(t) = \sum_j |h_{ji}(t)|$$

If this is larger than a threshold θ_ϕ, then the amount of PRP $\phi_j(t)$ increases at rate α_ϕ, while it decays otherwise:

$$\tau_\phi \frac{d\phi_j(t)}{dt} = -\phi_j(t) + \alpha_\phi \cdot \Theta(\mathrm{SPS}_j(t) - \theta_\phi) \tag{6}$$

Here, the timescale of the dynamics is given by the constant τ_ϕ.

Coupling of early-phase dynamics to the actin-based model of late-phase plasticity

The changes in the dynamics of actin-binding proteins during LTP and LTD are induced by calcium-dependent signaling cascades [31]. In particular, the signaling chain depending on calcineurin (CaN) is activated by intermediate calcium levels during LTD, whereas the signaling chain downstream of CaMKII is typically activated by very high calcium levels and triggers LTP in downstream signaling. Following this, in our integrated model, CaMKII and CaN are set to CaMKII $\equiv 1.0$ and CaN $\equiv 1.0$ whenever the calcium concentration fulfills $c(t) > \theta_{\mathrm{CaMKII}}$ and $c(t) > \theta_{\mathrm{d}}$, respectively (cf. Eq. 4).

Otherwise, the concentrations of CaMKII and CaN decay exponentially following

$$\frac{d\mathrm{CaMKII}_{ji}}{dt} = -\mathrm{CaMKII}_{ji}/\tau_{\mathrm{CaMKII}}, \qquad \frac{d\mathrm{CaN}_{ji}}{dt} = -\mathrm{CaN}_{ji}/\tau_{\mathrm{CaN}}. \tag{7}$$

Altered dynamics for the crosslinkers and the birth-death process are applied if one or both of the signals are above a threshold of 0.5. For simplicity, we do not explicitly simulate the birth-death process for actin foci in the full-integrated model, but instead use the expected mean values for n_{f} as given in Table 2. Thus, k_{b}, k_{u} and n_{f} for each synapse are set to the values for potentiation from Table 2 when CaMKII-signaling is on ($\mathrm{CaMKII}_{ji} > 0.5$), to the values for depression when only CaN-signaling is on ($\mathrm{CaMKII}_{ji} < 0.5$ and $\mathrm{CaN}_{ji} > 0.5$), and to the basal values otherwise.

Finally, in our integrated model, we use the PSD-dependent volume V_{PSD} as a proxy for the late-phase weight z (cf. [15, 59]), in the following way:

$$z(t) = c_w + \left(\frac{V_{\mathrm{PSD}}(t)}{V_{\mathrm{PSD}}(0)} - 1\right) \cdot c_w \cdot c_{\mathrm{late}}, \tag{8}$$

where c_w is a constant determining the unscaled initial weight and the weight dynamics, and c_{late} determines the ratio by which the late-phase weight enters the total weight. The late-phase weight is then added to the early-phase weight h to yield the total weight of the synapse:

$$w(t) = h(t) + z(t). \tag{9}$$

Neuronal circuit

To perform even more realistic investigations with our integrated model of early- and late-phase synaptic plasticity with the calcium traces driven by neuronal spikes, we consider the model in an actual neuronal circuit. Thus, we set up a small network of 4 neurons with the following connections: $0 \to 1$, $0 \to 2$, $0 \to 3$, $2 \to 3$, $3 \to 2$. We

stimulated neuron 0 as detailed in the next subsection. Depending on the stimulation protocol, plasticity was induced at all of the synapses, but for comparison with the abstracted model, we only report the results of the feed-forward synapse $0 \to 1$ here. Note that readers may use our freely provided program code to explore the dynamics of our plasticity model at all synapses in the circuit.

For weak-before-strong and strong-before-weak paradigms, we set up a small network of 3 neurons with the connections $1 \to 0$ and $2 \to 0$. In this context, neuron 1 received strong stimulation and neuron 2 received weak stimulation, as detailed in the next subsection.

For the neuron model, we used the leaky integrate-and-fire formalism, given by

$$\tau_{\text{mem}} \frac{dV_j(t)}{dt} = V^{\text{rev}} - V_j(t) + V_j^{\text{PSP}}(t) + V_j^{\text{stim}}(t), \tag{10}$$

for the neuron with index j. Here, V^{rev} is the reversal potential, τ_{mem} is the membrane time constant, $V_j^{\text{PSP}}(t)$ is the sum of postsynaptic potentials, and $V_j^{\text{stim}}(t)$ accounts for the external stimulation (see the following subsection). With the synaptic weights w_{ji} (see Eq. 9) and the set $S(i)$ of the presynaptic spike times, the postsynaptic potential is given by:

$$V_j^{\text{PSP}}(t) = \sum_i \sum_{t' \in S(i)} w_{ji} \cdot \exp\left(-\frac{t - t' - t_{\text{axd}}}{\tau_{\text{syn}}}\right) \cdot \Theta(t - t' - t_{\text{axd}}), \tag{11}$$

where t_{axd} is the axonal delay time, τ_{syn} is the synaptic time constant, and $\Theta(\cdot)$ is the Heaviside step function. A spike is triggered if the neuronal membrane voltage $V_j(t)$ crosses the threshold V^{th}, following which the membrane voltage is set to V^{reset}, where it remains for the refractory time t_{ref} (see Table 1 for the parameter values).

Stimulation protocols

To induce l-LTP, l-LTD, e-LTP only, and e-LTD only, we chose classical well-established stimulation protocols (cf. [14, 15, 47]). We conveyed these protocols by forcing a presynaptic neuron to spike with Poisson-distributed spike times, which can be used to model the firing of a neuron at a certain average rate (cf. [52]). The details of the protocols are described in the following.

Strong tetanic stimulation (STET). This protocol serves to induce l-LTP. It consists of three pulses of 100 Hz stimulation, each lasting for 1.00 s. The pulses are separated by breaks of 600 s.

Weak tetanic stimulation (WTET). This protocol serves to induce e-LTP. It consists of one pulse of 100 Hz stimulation, lasting for 0.20 s.

Strong low-frequency stimulation (SLFS). This protocol serves to induce l-LTD. It consists of 900 pulses of 20 Hz stimulation, each lasting for 0.15 s. The pulses are separated by breaks of 1.00 s.

Weak low-frequency stimulation (WLFS). This protocol serves to induce e-LTD. It consists of one long period of 1 Hz stimulation, lasting for 900 s.

Software

For the late-phase-only model, we used a custom Python implementation that was designed to enable easy switching between simulations paradigms.

The full-integrated model was implemented using the Arbor simulator library [60, 81], which is well suited for the efficient execution of simulations of networks of multi-compartment neurons on high-performance computing hardware, and will thus allow for future network simulations employing our model.

We will make our simulation code freely available upon publication of this article.

Supporting information

Appendix S1. Fixed-point and stability analysis for late-phase model

Acknowledgments

This work was supported by the German Research Foundation (Deutsche Forschungsgemeinschaft, DFG) through grants SFB1286 (projects C01, C03 and Z01).

Author contributions

Conceptualization: FN, JL, CT, MF; Formal Analysis: FN, JL, MF; Funding acquisition: MF, CT; Investigation: FN, JL, MF; Methodology: FN, JL, CT, MF; Project administration: CT, MF; Software: FN, JL; Supervision: CT, MF; Visualization: FN, JL, MF; Writing – original draft: JL, MF; Writing – review & editing: FN, JL, CT, MF.

References

1. Martin SJ, Grimwood PD, Morris RG. Synaptic plasticity and memory: an evaluation of the hypothesis. Annual review of neuroscience. 2000;23(1):649–711.
2. Bliss TV, Lømo T. Long-lasting potentiation of synaptic transmission in the dentate area of the anaesthetized rabbit following stimulation of the perforant path. The Journal of physiology. 1973;232(2):331–356.
3. Dudek SM, Bear MF. Homosynaptic long-term depression in area CA1 of hippocampus and effects of N-methyl-D-aspartate receptor blockade. Proceedings of the National Academy of Sciences. 1992;89(10):4363–4367.
4. Abraham WC. How long will long-term potentiation last? Philosophical Transactions of the Royal Society of London Series B: Biological Sciences. 2003;358(1432):735–744.
5. Frey U, Morris RG. Synaptic tagging and long-term potentiation. Nature. 1997;385(6616):533–536.
6. Redondo RL, Morris RGM. Making memories last: the synaptic tagging and capture hypothesis. Nature Reviews Neuroscience. 2011;12:17–30.
7. Staubli U, Lynch G. Stable depression of potentiated synaptic responses in the hippocampus with 1–5 Hz stimulation. Brain Research. 1990;513(1):113–118. doi:https://doi.org/10.1016/0006-8993(90)91096-Y.
8. Barrionuevo G, Schottler F, Lynch G. The effects of repetitive low frequency stimulation on control and "potentiated" synaptic responses in the hippocampus. Life sciences. 1980;27(24):2385–2391.
9. Chen YL, Huang CC, Hsu KS. Time-dependent reversal of long-term potentiation by low-frequency stimulation at the hippocampal mossy fiber–CA3 synapses. Journal of Neuroscience. 2001;21(11):3705–3714.

10. Huang CC, Liang YC, Hsu KS. Characterization of the Mechanism Underlying the Reversal of Long Term Potentiation by Low Frequency Stimulation at Hippocampal CA1 Synapses. Journal of Biological Chemistry. 2001;276(51):48108–48117. doi:https://doi.org/10.1074/jbc.M106388200.

11. Clopath C, Ziegler L, Vasilaki E, Büsing L, Gerstner W. Tag-Trigger-Consolidation: A Model of Early and Late Long-Term-Potentiation and Depression. PLOS Computational Biology. 2008;4(12):1–14. doi:10.1371/journal.pcbi.1000248.

12. Barrett AB, Billings GO, Morris RGM, van Rossum MCW. State Based Model of Long-Term Potentiation and Synaptic Tagging and Capture. PLOS Computational Biology. 2009;5(1):1–12. doi:10.1371/journal.pcbi.1000259.

13. Ziegler L, Zenke F, Kastner DB, Gerstner W. Synaptic consolidation: from synapses to behavioral modeling. Journal of Neuroscience. 2015;35(3):1319–1334.

14. Li Y, Kulvicius T, Tetzlaff C. Induction and consolidation of calcium-based homo-and heterosynaptic potentiation and depression. PLOS ONE. 2016;11(8):e0161679.

15. Luboeinski J, Tetzlaff C. Memory consolidation and improvement by synaptic tagging and capture in recurrent neural networks. Communications Biology. 2021;4(275). doi:10.1038/s42003-021-01778-y.

16. Ding Y, Wang Y, Cao L. A Simplified Plasticity Model Based on Synaptic Tagging and Capture Theory: Simplified STC. Frontiers in Computational Neuroscience. 2022;15. doi:10.3389/fncom.2021.798418.

17. Song S, Sjöström PJ, Reigl M, Nelson S, Chklovskii DB. Highly nonrandom features of synaptic connectivity in local cortical circuits. PLOS biology. 2005;3(3):e68.

18. Amit DJ, Gutfreund H, Sompolinsky H. Storing infinite numbers of patterns in a spin-glass model of neural networks. Physical Review Letters. 1985;55(14):1530.

19. Miller P, Zhabotinsky AM, Lisman JE, Wang XJ. The stability of a stochastic CaMKII switch: dependence on the number of enzyme molecules and protein turnover. PLOS biology. 2005;3(4):e107.

20. Pi HJ, Lisman JE. Coupled phosphatase and kinase switches produce the tristability required for long-term potentiation and long-term depression. Journal of Neuroscience. 2008;28(49):13132–13138.

21. Rangamani P, Levy MG, Khan S, Oster G. Paradoxical signaling regulates structural plasticity in dendritic spines. Proceedings of the National Academy of Sciences. 2016;113(36):E5298–E5307. doi:10.1073/pnas.1610391113.

22. Khan R, Kulasiri D, Samarasinghe S. A multifarious exploration of synaptic tagging and capture hypothesis in synaptic plasticity: Development of an integrated mathematical model and computational experiments. Journal of Theoretical Biology. 2023;556:111326. doi:https://doi.org/10.1016/j.jtbi.2022.111326.

23. Martin KC, Kosik KS. Synaptic tagging—who's it? Nature Reviews Neuroscience. 2002;3(10):813–820.

24. Pinho J, Marcut C, Fonseca R. Actin remodeling, the synaptic tag and the maintenance of synaptic plasticity. IUBMB life. 2020;72(4):577–589.

25. Mogilner A, Oster G. Cell motility driven by actin polymerization. Biophysical journal. 1996;71(6):3030–3045.

26. Fischer M, Kaech S, Knutti D, Matus A. Rapid actin-based plasticity in dendritic spines. Neuron. 1998;20(5):847–854.

27. Bonilla-Quintana M, Wörgötter F, Tetzlaff C, Fauth M. Modeling the shape of synaptic spines by their actin dynamics. Frontiers in synaptic neuroscience. 2020;12:9.

28. Bonilla-Quintana M, Wörgötter F, D'Este E, Tetzlaff C, Fauth M. Reproducing asymmetrical spine shape fluctuations in a model of actin dynamics predicts self-organized criticality. Scientific reports. 2021;11(1):4012.

29. Thomas M, Bogaciu CA, Rizzoli SO, Fauth M. Stable Actin As Synaptic Tag. bioRxiv. 2025;doi:10.1101/2025.02.10.637360.

30. Okamoto KI, Narayanan R, Lee SH, Murata K, Hayashi Y. The role of CaMKII as an F-actin-bundling protein crucial for maintenance of dendritic spine structure. Proceedings of the National Academy of Sciences. 2007;104(15):6418–6423. doi:10.1073/pnas.0701656104.

31. Borovac J, Bosch M, Okamoto K. Regulation of actin dynamics during structural plasticity of dendritic spines: Signaling messengers and actin-binding proteins. Molecular and Cellular Neuroscience. 2018;91:122–130.

32. Honkura N, Matsuzaki M, Noguchi J, Ellis-Davies GC, Kasai H. The subspine organization of actin fibers regulates the structure and plasticity of dendritic spines. Neuron. 2008;57(5):719–729.

33. Frost NA, Shroff H, Kong H, Betzig E, Blanpied TA. Single-molecule discrimination of discrete perisynaptic and distributed sites of actin filament assembly within dendritic spines. Neuron. 2010;67(1):86–99.

34. Bosch M, Castro J, Saneyoshi T, Matsuno H, Sur M, Hayashi Y. Structural and molecular remodeling of dendritic spine substructures during long-term potentiation. Neuron. 2014;82(2):444–459.

35. Bonilla-Quintana M, Wörgötter F. Exploring new roles for actin upon LTP induction in dendritic spines. Scientific Reports. 2021;11(1):7072.

36. Quintana MB, Rangamani P. Mechanical forces promote actin-mediated structural plasticity. Biophysical Journal. 2023;122(3):418a.

37. Holler S, Köstinger G, Martin KA, Schuhknecht GF, Stratford KJ. Structure and function of a neocortical synapse. Nature. 2021;591(7848):111–116.

38. Becker MFP, Tetzlaff C. The biophysical basis underlying the maintenance of early phase long-term potentiation. PLOS Computational Biology. 2021;17(3):e1008813.

39. Meyer D, Bonhoeffer T, Scheuss V. Balance and stability of synaptic structures during synaptic plasticity. Neuron. 2014;82(2):430–443.

40. Clavet-Fournier V, Lee C, Wegner W, Brose N, Rhee J, Willig KI. Pre- and postsynaptic nanostructures increase in size and complexity after LTP induction. bioRxiv. 2023;doi:10.1101/2023.02.09.527812.

41. Matsuzaki M, Honkura N, Ellis-Davies GC, Kasai H. Structural basis of long-term potentiation in single dendritic spines. Nature. 2004;429(6993):761–766.

42. Noguchi J, Hayama T, Watanabe S, Ucar H, Yagishita S, Takahashi N, et al. State-dependent diffusion of actin-depolymerizing factor/cofilin underlies the enlargement and shrinkage of dendritic spines. Scientific reports. 2016;6:32897. doi:10.1038/srep32897.

43. Sekino Y, Koganezawa N, Mizui T, Shirao T. Role of drebrin in synaptic plasticity. Drebrin: From Structure and Function to Physiological and Pathological Roles. 2017; p. 183–201.

44. Yasuda H, Kojima N, Hanamura K, Yamazaki H, Sakimura K, Shirao T. Drebrin isoforms critically regulate NMDAR-and mGluR-dependent LTD induction. Frontiers in Cellular Neuroscience. 2018;12:330.

45. Kasai H, Ziv NE, Okazaki H, Yagishita S, Toyoizumi T. Spine dynamics in the brain, mental disorders and artificial neural networks. Nature Reviews Neuroscience. 2021;22(7):407–422.

46. Graupner M, Brunel N. Calcium-based plasticity model explains sensitivity of synaptic changes to spike pattern, rate, and dendritic location. Proceedings of the National Academy of Sciences. 2012;109(10):3991–3996.

47. Sajikumar S, Navakkode S, Sacktor TC, Frey JU. Synaptic tagging and cross-tagging: the role of protein kinase Mζ in maintaining long-term potentiation but not long-term depression. Journal of Neuroscience. 2005;25(24):5750–5756.

48. Frey U, Morris RG. Synaptic tagging: implications for late maintenance of hippocampal long-term potentiation. Trends in neurosciences. 1998;21(5):181–188.

49. Kramár EA, Babayan AH, Gavin CF, Cox CD, Jafari M, Gall CM, et al. Synaptic evidence for the efficacy of spaced learning. Proceedings of the National Academy of Sciences. 2012;109(13):5121–5126.

50. Smolen P, Zhang Y, Byrne JH. The right time to learn: mechanisms and optimization of spaced learning. Nature Reviews Neuroscience. 2016;17(2):77.

51. Yang Y, Wang Xb, Frerking M, Zhou Q. Spine expansion and stabilization associated with long-term potentiation. Journal of Neuroscience. 2008;28(22):5740–5751.

52. Dayan P, Abbott LF. Theoretical Neuroscience. 1st ed. Cambridge/MA, USA: The MIT Press; 2001.

53. Pache A, van Rossum MC. Energetically efficient learning in neuronal networks. Current opinion in neurobiology. 2023;83:102779.

54. Li HL, Van Rossum MC. Energy efficient synaptic plasticity. Elife. 2020;9:e50804.

55. Gardner-Medwin AR. Doubly modifiable synapses: a model of short and long term auto-associative memory. Proceedings of the Royal Society B. 1989;238(1291):137–154.

56. Fusi S, Drew PJ, Abbott LF. Cascade models of synaptically stored memories. Neuron. 2005;45(4):599–611.

57. Päpper M, Kempter R, Leibold C. Synaptic tagging, evaluation of memories, and the distal reward problem. Learning & Memory. 2011;18:58–70.

58. Benna MK, Fusi S. Computational principles of synaptic memory consolidation. Nature neuroscience. 2016;19(12):1697–1706.

59. Luboeinski J, Tetzlaff C. Organization and priming of long-term memory representations with two-phase plasticity. Cognitive Computation. 2022;doi:10.1007/s12559-022-10021-7.

60. Luboeinski J, Schmitt S, Shafiee S, Hater T, Bösch F, Tetzlaff C. Plastic Arbor: a modern simulation framework for synaptic plasticity – from single synapses to networks of morphological neurons. Preprint at arXiv. 2024;2411.16445.

61. Lehr AB, Luboeinski J, Tetzlaff C. Neuromodulator-dependent synaptic tagging and capture retroactively controls neural coding in spiking neural networks. Scientific Reports. 2022;12:17772.

62. Kastellakis G, Silva AJ, Poirazi P. Linking memories across time via neuronal and dendritic overlaps in model neurons with active dendrites. Cell Reports. 2016;17(6):1491–1504.

63. Luboeinski J, Tetzlaff C. Modeling Emergent Dynamics Arising from Synaptic Tagging and Capture at the Network Level. In: Sajikumar S, Abel T, editors. Synaptic Tagging and Capture: From Synapses to Behavior. 2nd ed. Cham, Switzerland: Springer; 2024. p. 471–503.

64. Kim K, Lakhanpal G, Lu H, Khan M, Suzuki A, Kato Hayashi M, et al. A Temporary Gating of Actin Remodeling during Synaptic Plasticity Consists of the Interplay between the Kinase and Structural Functions of CaMKII. Neuron. 2015;87(4):813–826. doi:https://doi.org/10.1016/j.neuron.2015.07.023.

65. Fujii H, Inoue M, Okuno H, Sano Y, Takemoto-Kimura S, Kitamura K, et al. Nonlinear decoding and asymmetric representation of neuronal input information by CaMKIIα and calcineurin. Cell reports. 2013;3(4):978–987.

66. Gerstner W, Kistler WM. Spiking Neuron Models. 1st ed. Cambridge, UK: Cambridge University Press; 2002.

67. Roth A, van Rossum MCW. Modeling Synapses. In: De Schutter E, editor. Computational Modeling Methods for Neuroscientists. 1st ed. Cambridge/MA, USA: MIT Press; 2009.

68. Lin JW, Faber DS. Modulation of synaptic delay during synaptic plasticity. Trends in Neurosciences. 2002;25(9):449–455.

69. Kobayashi R, Tsubo Y, Shinomoto S. Made-to-Order Spiking Neuron Model Equipped with a Multi-Timescale Adaptive Threshold. Frontiers in Computational Neuroscience. 2009;3(9).

70. Fonseca R. Activity-dependent actin dynamics are required for the maintenance of long-term plasticity and for synaptic capture. European Journal of Neuroscience. 2012;35(2):195–206.

71. Szabó EC, Manguinhas R, Fonseca R. The interplay between neuronal activity and actin dynamics mimic the setting of an LTD synaptic tag. Scientific reports. 2016;6(1):33685.

72. Lee SJR, Escobedo-Lozoya Y, Szatmari EM, Yasuda R. Activation of CaMKII in single dendritic spines during long-term potentiation. Nature. 2009;458(7236):299–304.

73. Nogueira F. Bayesian Optimization: Open source constrained global optimization tool for Python; 2014–. Available from: `https://github.com/bayesian-optimization/BayesianOptimization`.

74. Zhou Q, Homma KJ, ming Poo M. Shrinkage of Dendritic Spines Associated with Long-Term Depression of Hippocampal Synapses. Neuron. 2004;44(5):749–757. doi:https://doi.org/10.1016/j.neuron.2004.11.011.

75. Henley JM, Wilkinson KA. Synaptic AMPA receptor composition in development, plasticity and disease. Nature Reviews Neuroscience. 2016;17(6):337–350.

76. Bliss TV, Collingridge GL. A synaptic model of memory: long-term potentiation in the hippocampus. Nature. 1993;361(6407):31.

77. Sajikumar S, Navakkode S, Frey JU. Identification of compartment- and process-specific molecules required for "synaptic tagging" during long-term potentiation and long-term depression in hippocampal CA1. Journal of Neuroscience. 2007;27(19):5068–5080.

78. Govindarajan A, Israely I, Huang SY, Tonegawa S. The dendritic branch is the preferred integrative unit for protein synthesis-dependent LTP. Neuron. 2011;69(1):132–146.

79. Glock C, Heumüller M, Schuman EM. mRNA transport & local translation in neurons. Current Opinion in Neurobiology. 2017;45:169–177.

80. Sun C, Nold A, Fusco CM, Rangaraju V, Tchumatchenko T, Heilemann M, et al. The prevalence and specificity of local protein synthesis during neuronal synaptic plasticity. Science Advances. 2021;7(38):eabj0790.

81. Akar NA, Biddiscombe J, Cumming B, Kabic M, Karakasis V, Klijn W, et al. Arbor Library v0.9.0; 2023. Available from: `https://doi.org/10.5281/zenodo.8233847`.

Appendix S1: Analysis of stable states and their stability

Here, we want to calculate the fixed points of our model under constant parameter values and analyze their stability. For this we first replace the stochastic birth death process that determines the number of foci with the current expected value, corresponding to the temporal mean $\langle n_\mathrm{f} \rangle$, to arrive at a non-stochastic dynamic system. We further simplify the calculation by defining $V_\mathrm{tot} = V_\mathrm{d} + V_\mathrm{s}$ and only investigate the dynamic of two dimensional system. When the crosslinker binding and unbinding are in equilibrium, the dynamic and stable pool can then be obtained as fractions of V_tot:

$$V_\mathrm{d}^* = \frac{k_\mathrm{u}}{k_\mathrm{b} + k_\mathrm{u}} V_\mathrm{tot} \ , \tag{12}$$

$$V_\mathrm{s}^* = \frac{k_\mathrm{b}}{k_\mathrm{b} + k_\mathrm{u}} V_\mathrm{tot}. \tag{13}$$

We arrive at

$$\frac{dV_\mathrm{tot}}{dt} = k_\mathrm{growth} \langle n_\mathrm{f} \rangle - k_\mathrm{decay} \left[\frac{k_\mathrm{b}}{k_\mathrm{b} + k_\mathrm{u}} - c_0 \right]_+ [V_\mathrm{tot} - V_\mathrm{PSD}]_+$$

Assuming that both rectifications are in their linear regime, we obtain a fixed-point for V_tot that can be expressed as function of V_PSD:

$$V_\mathrm{tot}^* = V_\mathrm{PSD}^* + \frac{k_\mathrm{growth} \cdot \langle n_\mathrm{f} \rangle}{k_\mathrm{decay}} \left(\frac{k_\mathrm{u}}{k_\mathrm{b} + k_\mathrm{u}} - c_0 \right)^{-1}. \tag{14}$$

This is a continuous line of fixed points in the $V_\mathrm{tot} - V_\mathrm{PSD}$-space.

In order to compute the stability of these fixed points, we first compute the Jacobian matrix of our equations evaluated at the fixed point:

$$J = \begin{pmatrix} -k_\mathrm{decay} \left(\frac{k_\mathrm{u}}{k_\mathrm{b}+k_\mathrm{u}} - c_0 \right) & k_\mathrm{decay} \left(\frac{k_\mathrm{u}}{k_\mathrm{b}+k_\mathrm{u}} - c_0 \right) \\ \frac{1}{\tau_\mathrm{PSD}} & -\frac{1}{\tau_\mathrm{PSD}} \end{pmatrix}.$$

The resulting Eigenvalues are $\lambda_1 = 0$ and $\lambda_2 = -k_\mathrm{decay} \left(\frac{k_\mathrm{u}}{k_\mathrm{b}+k_\mathrm{u}} - c_0 \right) - \frac{1}{\tau_\mathrm{PSD}}$. Hereby, the Eigenvector for λ_1 is proportional to $(1,1)^T$ and thus aligns with the line of fixed-points. This proves that the fixed-point manifold defined by equation 14 forms a stable line-attractor.